Redistribution of high energy alpha particles due to sawteeth with partial reconnection

2013 Nucl. Fusion 53 043012

(http://iopscience.iop.org/0029-5515/53/4/043012)

IOP Publishing and International Atomic Energy Agency Nuclear Fusion
Nucl. Fusion **53** (2013) 043012 (11pp) doi:10.1088/0029-5515/53/4/043012

Redistribution of high energy alpha particles due to sawteeth with partial reconnection

R. Farengo[1], H.E. Ferrari[1,2], P.L. García-Martínez[2], M.-C. Firpo[3], W. Ettoumi[3] and A.F. Lifschitz[4]

[1] Comisión Nacional de Energía Atómica, Centro Atómico Bariloche e Instituto Balseiro, Bariloche, Argentina
[2] Consejo Nacional de Investigaciones Científicas y Técnicas (CONICET), Bariloche, Argentina
[3] Laboratoire de Physique des Plasmas, CNRS-Ecole Polytechnique-Paris VI, Palaiseau, France
[4] Laboratoire d'Optique Apliquée, ENSTA-CNRS-Ecole Polytechnique, Palaiseau, France

Received 12 November 2012, accepted for publication 28 February 2013
Published 28 March 2013
Online at stacks.iop.org/NF/53/043012

Abstract
The redistribution of high energy alpha particles due to internal kink modes is studied in plasmas with ITER-like parameters. The exact particle trajectories in the total fields, equilibrium plus perturbation, are calculated. The equilibrium magnetic field is obtained by analytically solving the Grad–Shafranov equation and the perturbed electric and magnetic fields are reconstructed using ideal MHD and the experimental information about the displacement eigenfunction. The (1, 1), (2, 2) and (2, 1) modes are included and the effect of changing their amplitude and frequency is determined. The results show that if the conditions are similar to those reported in Igochine *et al* (2007 *Nucl. Fusion* **47** 23), the peak density of counter-passing particles decreases between 25% and 40% (depending on the energy); the peak of the trapped particles density shifts outwards by approximately 10% of the minor radius and the total on axis density decreases by more than 25%. This redistribution occurs inside the $q = 1$ surface. The addition of a (2, 1) mode, which can produce the stochastization of the magnetic field, significantly increases particle redistribution and allows particles to spread beyond the $q = 1$ surface. Different groups of particles (co-passing, counter-passing, trapped) respond differently to the perturbations.

(Some figures may appear in colour only in the online journal)

1. Introduction

Sawtooth oscillations can produce a significant redistribution of the alpha particle population. This is particularly important in ITER, and future fusion reactors, because it will modify the power deposition profile and can increase alpha particle losses and wall loading. In addition, alpha particle transport from the core to the outer region can trigger other instabilities. The redistribution of suprathermal particles (beam ions, fusion products, etc) in sawteeth has been clearly demonstrated in various experiments [1–6].

Although the most basic features of sawteeth, such as the presence of a kink mode, are common to all experiments, other aspects can vary, depending on the device and the discharge conditions. The amount of reconnected flux and the values of the safety factor (on axis, q_0) and the amplitude of the kink mode after the crash are examples of quantities that can present significant variations. Theoretical models of sawteeth also present significant differences. The initial model proposed by Kadomtsev [7] assumed full reconnection and predicted $q_0 \geqslant 1$ and no kink mode after the crash. An alternative model proposed by Kolesnichenko *et al* [8] assumes full reconnection but allows for $q_0 < 1$ after the crash, provided that two current layers arise. Models with partial reconnection, which assume that the reconnection stops at some inner radius, have also been proposed [9]. Recently, a series of studies conducted in the ASDEX-Upgrade tokamak [10–13] showed that in this device sawteeth are characterized by the following features: (i) partial reconnection; (ii) $q_0 < 1$ after the crash and (iii) survival of the kink mode, which drops to 40% of its maximum amplitude at the crash and slowly decays afterwards. Since none of the above referenced models can explain all of these features the hypothesis that stochasticity plays an important role in ASDEX-U sawteeth was introduced. Unfortunately, no reliable numerical simulations of the entire sawtooth process that can predict the experimental results are available.

Theoretical studies of alpha particle redistribution due to sawteeth can be broadly classified in two groups. One

group includes those studies that assume full reconnection and employ a phenomenological description of the evolution of the flux surfaces, generally including only the dominant (1,1) kink mode. The other group includes the studies that directly employ the information about the spatial and temporal evolution of the modes present in a sawtooth to calculate the trajectories of the alpha particles [14, 15]. The approach employed in the studies included in the first group appears to be better suited for sawteeth that exhibit full reconnection while the one used in those included in the second group provides a more accurate description of the dynamics of alpha particles in sawteeth with partial reconnection and can include the effect of field line stochasticity.

Initial studies in the first group assumed that the particles were tied to the flux surfaces, and moved with them [16]. Later, the importance of the electric field associated with the kink modes was recognized and incorporated in the calculations [17]. A critical energy was also found [17], above which the perturbation has little effect on particle motion. An overview of previous results together with an analysis of the resonance between the electromagnetic fields of the sawtooth and particles having large orbit widths was presented in [18]. Finally, the effect of high β (ratio of plasma to magnetic pressure) was also studied [19].

The second approach requires knowing the space and time dependence of the electric and magnetic fields associated with the modes present in sawteeth and calculating the trajectories of a large number of particles. It has been employed by Zhao and White [14] and Farengo *et al* [15] and it is used in this study. The electric and magnetic fields can be obtained from theoretical calculations and/or numerical simulations, or from the experimental information. A method to employ the experimental information was introduced in [15] and is used here. The main assumptions and advantages of our method, and the differences with [14], are discussed in [15].

The experimental studies on the effect of sawteeth on alpha particle confinement indicated above [1–6] do not provide much information about the space and time dependence of the perturbed fields that produce the redistribution. In fact, there is little experimental information about the space and time dependence of the modes present in a sawtooth. We therefore employ the information provided in [12] and also study the effect of including modes not reported in [12]. In [15] the method was introduced and applied to study the diffusion of particles initially located on a given flux surface. Here we consider all the particles of a given energy. We present a systematic study of the effect of changing the number of modes, their amplitudes and frequencies, and the energy of the particles. The results show that if the conditions are similar to those reported in [12], the peak density of counter-passing particles decreases between 25% and 40% (depending on the energy); the peak of the trapped particles density shifts outwards by approximately 10% of the minor radius and the total on axis density decreases by more than 25%. This redistribution occurs inside the $q = 1$ surface. The addition of a (2, 1) mode, which can produce the stochastization of the magnetic field, significantly increases particle redistribution and allows particles to spread beyond the $q = 1$ surface. Finally, counter-passing particles are more strongly redistributed than co-passing particles while trapped particles spread out and move towards larger radii.

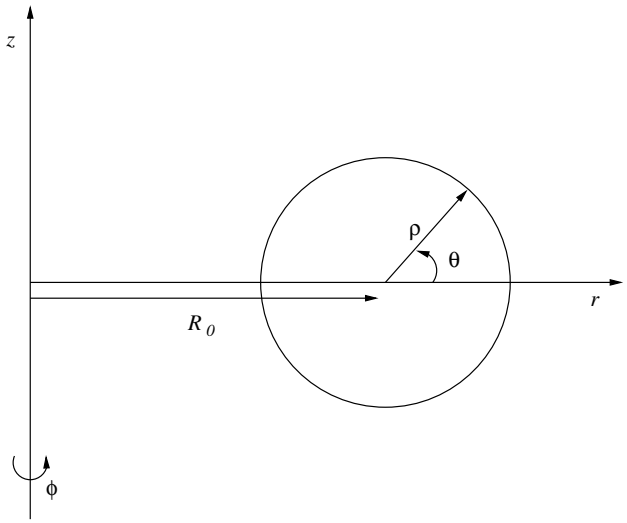

Figure 1. Coordinate systems.

The structure of this paper is as follows. In section 2 we briefly review the method introduced in [15] to calculate the fields and in section 3 the method employed to determine the initial conditions and calculate the trajectories of the particles. Section 4 contains the results of the numerical calculations. Finally, in section 5 we summarize our findings and discuss future research on this topic.

2. Equilibrium and perturbed fields

Here we briefly review the method employed in [15] to calculate the equilibrium and perturbed fields. A complete justification of the assumptions and approximations employed in the calculation can be found in that reference.

Two coordinate systems are employed: cylindrical and toroidal. Both systems are indicated in figure 1, where r, ϕ and z are the cylindrical coordinates, R_0 indicates the position of the geometric axis and ρ and θ are the toroidal coordinates ($r = R_0 + \rho\cos\theta$, $z = \rho\sin\theta$). The poloidal flux is obtained by expanding the Grad–Shafranov equation in powers of the inverse aspect ratio and assuming that the pressure and poloidal current depend on the poloidal flux as

$$p = p_1\psi^2; \qquad I^2 = I_0^2 + I_1^2\psi^2,$$

where ψ is the poloidal flux and p_1, I_0^2 and I_1^2 are constants (Gaussian units are used). Introducing dimensionless quantities and keeping only the first two terms in the expansion the poloidal flux of an equilibrium with circular cross section can be written as [15]

$$\psi(x,\theta) = C\left\{J_0(kx) + \frac{\cos\theta}{2} \times \left[xJ_0(kx) + \frac{\sigma J_1(kx)}{k}\left(1-x^2\right)\right]\right\}, \quad (1)$$

where x is the normalized minor radius coordinate ($x = \rho/a$, a: minor radius), θ is the poloidal angle and $J_0(kx)$ and $J_1(kx)$ are Bessel functions. The poloidal flux is normalized with $B_0\pi a^2$, where B_0 is the external toroidal field at the geometric axis (R_0), p is normalized with $B_0^2/8\pi$ and I with $B_0cR_0/2$.

The other quantities appearing in equation (1) are $\sigma = 4p_1/\varepsilon^2$ and $k^2 = 4(p_1 + I_1^2)/\varepsilon^2$, where ε is the inverse aspect ratio. The boundary of the plasma is at the $x = 1$ surface, where we request the flux to be zero. The constant C is determined by fixing the poloidal field at the plasma boundary (total toroidal plasma current) and I_0 is related to the vacuum toroidal field. Since we normalize all the fields with the vacuum toroidal field at R_0, $I_0 = 1$. Finally, σ, which is proportional to p_1, fixes the plasma β. Knowing the poloidal flux we can calculate the equilibrium magnetic field. Figure 2 of [15] shows the q profile and flux surfaces obtained with $\varepsilon = 1/3$, $p_1 = 0.05$ and $B_{\rm pol}(x = 1, \theta = 0) = 0.155$ ($q_0 = 0.83$). Note that a positive poloidal field at the outer boundary means a negative toroidal current (antiparallel to the toroidal field).

Ideal MHD is used to calculate the perturbed electric and magnetic fields:

$$\boldsymbol{B}_1 = \nabla \times (\boldsymbol{\xi} \times \boldsymbol{B}), \qquad \boldsymbol{E}_1 = -\frac{\boldsymbol{v}_1 \times \boldsymbol{B}}{c}, \qquad \boldsymbol{v}_1 = \frac{\partial \boldsymbol{\xi}}{\partial t}, \tag{2}$$

where $\boldsymbol{E}_1$ and $\boldsymbol{B}_1$ are the normalized (with B_0) perturbed electric and magnetic fields, $\boldsymbol{\xi}$ is the displacement, normalized with the minor radius (a) and $\boldsymbol{B}$ is the normalized equilibrium magnetic field.

Reference [12] reports the presence of the (1, 1), (2, 2) and (3, 3) modes during sawteeth, where the first digit indicates the poloidal mode number (m) and the second the toroidal one (n). The amplitude of the (1, 1) mode goes to zero at the $q = 1$ surface while the (2, 2) mode extends, with very small amplitude, a little beyond this surface. The amplitude of the (3, 3) mode is very small everywhere. Under these conditions, including only the (1, 1) and (2, 2) modes, as was done in [15], has two consequences:

(i) The redistribution of alpha particles cannot go much beyond the $q = 1$ surface, where the modes disappear.
(ii) The magnetic field cannot become stochastic.

The second consequence can be understood by noting that the equations for the magnetic field lines can be cast in the Hamiltonian form. For tokamaks, the Hamiltonian is the poloidal magnetic flux and reads

$$H(\psi_t, \theta, \phi) = H_0(\psi_t) + \sum_{m,n} H_{mn}(\psi_t) \cos(m\theta - n\phi + \chi_{mn}), \tag{3}$$

where ϕ is the toroidal angle, $H_0(\psi_t) = \int^{\psi_t} 1/q(\psi')\,\mathrm{d}\psi'$ and ψ_t is the toroidal magnetic flux, conjugated to the poloidal angle θ. If one assumes that only $m = n$ modes are present, then the corresponding Hamiltonian, (3), can easily be shown to be integrable through a canonical change of variables, with the generating function $F_2(\psi_t, \theta, \phi) = (\theta - \phi)\psi_t$, that amounts to moving to the (1, 1) wave frame.

Introducing a different helicity, here through the (2, 1) mode, is required for the magnetic field lines deriving from (3) to become stochastic [20]. In [14] the (1, 1), (2, 1) and (4, 3) modes are included, and it is concluded that stochasticity can be important in the redistribution of the alpha particles. Here we will study the effect of the (1, 1), (2, 2) and (2, 1) modes. The x component of the displacement is therefore written as

$$\begin{aligned}\xi_x(x, \phi, \theta, t) = {} & \xi^{11}(t) f_{11}(x) \cos(\theta - \phi - \omega_{11} t) \\ & + \xi^{22}(t) f_{22}(x) \cos[2(\theta - \phi - \omega_{11} t)] \\ & + \xi^{21}(t) f_{21}(x) \cos(2\theta - \phi - \omega_{21} t),\end{aligned} \tag{4}$$

where ω_{11} and ω_{21} are the frequency of oscillation of the (1, 1) and (2, 1) modes and $\xi^{mn}(t)$ and $f_{mn}(x)$ are chosen to match the space and time dependence observed in the experiments. The spatial structure and temporal variation of the (1, 1) and (2, 2) modes are obtained from the experimental information provided in [12] while the (2, 1) mode is obtained from [14]. The ratio ω_{21}/ω_{11} is fixed at 2.65, which is the value reported in [14].

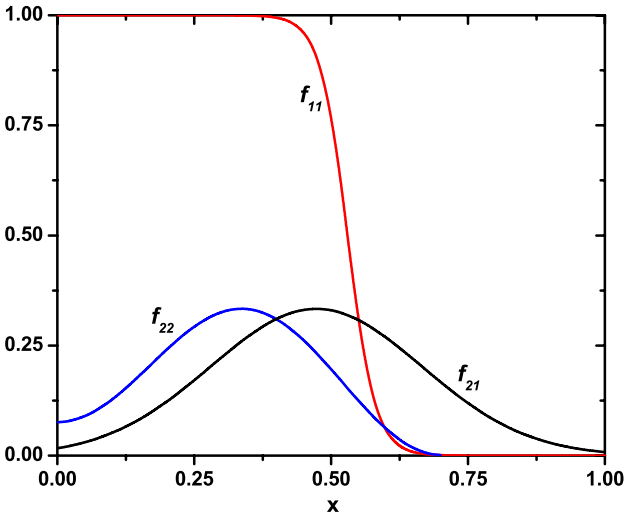

Figure 2. Spatial structure of the (1, 1), (2, 2) and (2, 1) modes.

Considering incompressible displacements ($\nabla \cdot \boldsymbol{\xi} = 0$) and minimizing the change in potential energy for internal modes we can write the other components of $\boldsymbol{\xi}$ in terms of ξ_x [21] and use equation (2) to calculate the perturbed fields. To proceed we need to specify $\xi^{mn}(t)$ and $f_{mn}(x)$. We introduce the following $f_{mn}(x)$:

$$f_{11}(x) = \frac{1}{2}\{1 - \tanh[\delta(x - x_s)]\},$$

$$f_{22}(x) = \begin{cases} \cos^2\left[\dfrac{\pi}{2}\left(\dfrac{x - x_{22}}{x_{22}}\right)\right] + \dfrac{\mathrm{e}^{-x^2/x_{22}^2}}{4}, & x \leqslant 2x_{22}, \\ 0, & x > 2x_{22}, \end{cases}$$

$$f_{21}(x) = \exp\left\{-\frac{(x - x_{21}/2)^2}{(0.2888\, x_{21})^2}\right\},$$

where x_s is the (minor) radius of the $q = 1$ surface, $x_{22} \simeq 0.35$, x_{21} is the radius of the $q = 2$ surface ($x_{21} = 0.946$) and δ is a numerical constant adjusted to get the desired slope of the (1, 1) eigenfuction at $x = x_s$ (typically $\delta \geqslant 20$). Figure 2 shows the profiles of $f_{11}(x)$, $f_{22}(x)$ and $f_{21}(x)$.

The results presented in [12] indicate that the evolution of the (1, 1) mode has three different stages: a slow rise before the crash; a rapid drop, to approximately 40% of its peak amplitude, at the crash and a slow decay afterwards. The (2, 2) mode begins to grow when the (1, 1) mode has an amplitude

which is approximately 70% of its maximum value (see figure 3 in [12]) and decays to a small amplitude after the crash. When the (2, 1) mode is included, we use the same time dependence as for the (2, 2) mode. In most of our simulations we follow the particles from the time the (2, 2) mode begins to grow (or the (1, 1) mode is at 70% of its maximum amplitude if the (2, 2) mode is not included), go through the crash and continue until the (1, 1) mode has dropped to 40% of its initial amplitude. The method employed to specify the temporal dependence of the amplitude of the modes is similar to the one employed in [14, 15]. The explicit time dependences employed are

Growth phase:

$$\xi^{11}(t) = \xi_0^{11}\left[c_1 + \frac{\exp\{t/(c_2 t_c)\} - 1}{e-1}\right], \qquad 0 < t \leqslant t_c,$$

$$\xi^{22}(t) = \xi_0^{22}\frac{\left[\exp\{t/t_c\} - 1\right]}{e-1}, \qquad 0 < t \leqslant t_c,$$

$$\xi^{21}(t) = \xi_0^{21}\frac{\left[\exp\{t/t_c\} - 1\right]}{e-1}, \qquad 0 < t \leqslant t_c,$$

where t_c is the crash time and c_1 and c_2 are numerical constants, chosen to obtain the desired amplitudes at $t = 0$ and $t = t_c$. Setting $c_1 = 0.7$ and $c_2 = 2.4054$, the amplitude of the (1, 1) mode is $0.7\xi_0^{11}$ at $t = 0$ and ξ_0^{11} at $t = t_c$. The (2, 2) and (2, 1) modes begin to grow at $t = 0$ and reach their maximum value at $t = t_c$. Note that their amplitudes can be different. According to figure 3 of [12], the (2, 2) mode begins to grow approximately 1.5×10^{-3} s before the crash; we therefore set $t_c = 3.8 \times 10^5$, where the time has been normalized with the cyclotron frequency of an alpha particle in the external toroidal field at the geometric axis ($\Omega_\alpha = 2.54 \times 10^8\ \mathrm{s}^{-1}$).

Decay phase:

$$\xi^{11}(t) = \xi_0^{11}\left\{\frac{\left[\exp\{(t_c + t_{11} - t)/t_{11}\} - 1\right]}{e-1}\right\}, \qquad t_c < t \leqslant t_f,$$

$$\xi^{22}(t) = \xi_0^{22}\frac{\left[\exp\{(t_c + t_{22} - t)/t_{22}\} - 1\right]}{e-1}, \qquad t_c < t \leqslant t_f,$$

$$\xi^{21}(t) = \xi_0^{21}\frac{\left[\exp\{(t_c + t_{21} - t)/t_{21}\} - 1\right]}{e-1}, \qquad t_c < t \leqslant t_f,$$

where t_{11}, t_{22} and t_{21} are the decay times of the (1, 1), (2, 2) and (2, 1) modes, respectively. In all of our calculations we employed $t_{11} = 15\,\mu$s and $t_{22} = t_{21} = t_{11} \times 0.6$. Finally, t_f is chosen as the time (after the crash) it takes the (1, 1) mode to drop to 40% of its maximum amplitude (the (2, 2) and (2, 1) modes decay to 20% of their maximum amplitude). Figure 3 shows plots of $\xi^{11}(t)$ and $\xi^{22}(t)$, for $\xi_0^{22}/\xi_0^{11} = 1/3$ (the temporal dependence is the same for the (2, 2) and (2, 1) modes). Two additional curves (in black) are included in this figure; they correspond to different growth scenarios for the (1, 1) mode and were used to check the sensitivity of the results to the time history of the (1, 1) mode amplitude (see below).

To conclude this section we note that the analytic equilibrium employed is static. There are no flows, and therefore no sheared flows. It is well known that sheared flows can reduce fluctuations driven transport by reducing the correlation length in the direction of the shear [22]. Since our equilibrium is static alpha particle redistribution is not limited by this effect.

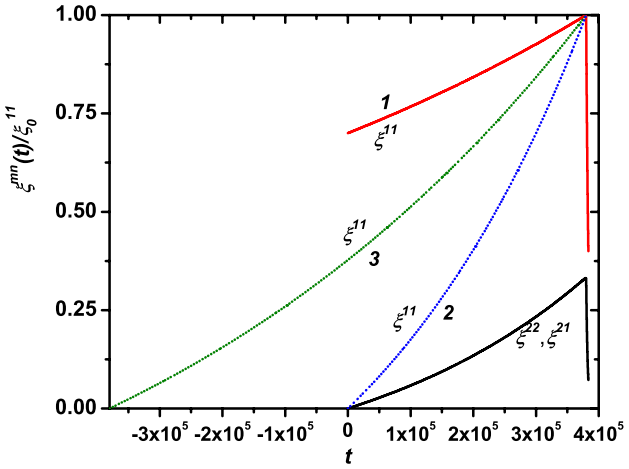

Figure 3. Temporal evolution of the modes. Three different growth scenarios are shown for the (1, 1) mode.

3. Initial conditions and numerical methods

The exact trajectories of a large number of alpha particles (typically 10^5) are followed to determine the redistribution produced by the modes considered. The high energy alpha particles are assumed to be initially distributed according to the slowing down distribution function:

$$F_s(r, v) = \begin{cases} \dfrac{S(r)\tau_s}{4\pi\left(v^3 + v_c^3\right)}, & v < v_0, \\ 0, & v > v_0, \end{cases}$$

where $S(r)$ is the source rate, τ_s is the slowing down time, v_c is the crossover velocity (equal friction with electrons and ions) and v_0 is the initial alpha particle velocity. The expressions for τ_s and v_c are the same employed in [23] while the fusion reaction rate was obtained using the accurate expression provided in [24]. The density of alpha particles with energies between E_1 and E_2 is obtained by integrating F_s between v_1 and v_2 ($v_{1,2} = (2E_{1,2}/m_\alpha)^{1/2}$):

$$n_\alpha(E_1, E_2) = \int_{v_1}^{v_2} F_s\, 4\pi v^2\, \mathrm{d}v = \frac{S\,\tau_s}{3}\left\{\ln\left(\frac{v_2^3}{v_c^3} + 1\right) - \ln\left(\frac{v_1^3}{v_c^3} + 1\right)\right\}.$$

The density of particles within a very narrow energy interval is obtained by assuming that $v_1 = v_2 - \delta$, with δ very small:

$$n_\alpha(E_1, E_2) \simeq \frac{S\,\tau_s\, v_2^2\,\delta}{\left(v_2^3 + v_c^3\right)}.$$

In our calculation v_2 is taken to be the velocity corresponding to the energy considered (i.e. $v_2 = (2E/m_\alpha)^{1/2}$, where E is the energy considered) and the value of δ is irrelevant because all we need is the spatial dependence for a given energy. To proceed we need to specify the density and temperature profiles. For standard ITER operating conditions, the density profile in the central region is expected to be quite flat and the temperature profile (before sawteeth) more peaked (see figure 91 of [25]). We therefore assume a uniform density profile, with $n_e = 1.2 \times 10^{14}\ \mathrm{cm}^{-3}$, and obtain the temperature profile from the pressure profile corresponding to our equilibrium, with $T_{e0} = T_{i0} = 18$ keV.

Knowing the alpha particle density profile, the following procedure is employed to determine the initial conditions of the alpha particles:

(i) The energy of the particle (absolute value of the initial velocity) is fixed ($E_0 \leqslant 3.5\,\mathrm{MeV}$).
(ii) A random initial position, distributed according to the alpha particle density, is chosen in the poloidal plane. For a normalized (with Ω_α) frequency of 2×10^{-4}, which is the value used in most simulations, the simulation time is more than 10 periods of the (1, 1) mode and therefore the initial toroidal location, which defines the initial phase at the position of the particle, is irrelevant.
(iii) A random (isotropic) initial velocity direction is chosen.

A low dissipation, fourth order, Runge–Kutta method [26] is employed to calculate the exact particle trajectories in the time dependent fields. Collisions are not included because the simulation time is much shorter than the collision time. The time step is taken small enough to guarantee that, when the perturbed fields are not included, the energy and azimuthal (toroidal) component of the canonical momentum (P_ϕ) are conserved (error less than 1%). In the equations of motion the time is normalized with Ω_α (defined above), lengths are normalized with the minor radius (a) and velocities with the initial velocity of the alpha particle (v_2). This results in a single dimensionless parameter appearing in the normalized equations:

$$\gamma = \frac{v_2}{\Omega_\alpha a}.$$

With ITER-like parameters ($B_0 = 5.3\,\mathrm{T}$, $a = 2\,\mathrm{m}$), $\gamma = 2.552 \times 10^{-2}$ for a 3.5 MeV alpha particle and decreases as the square root of the energy for lower energies.

To check that the number of particles employed in a standard simulation is sufficient, we repeated one case using four different sets of initial conditions, each with 10^5 particles. The difference between the maximum and minimum values of the parameter χ, which measures the spreading of the alpha particles (see definition below), resulted approximately 3%.

4. Results

In [15] we studied the effect of modes (1, 1) and (2, 2) on particles initially located on a given flux surface. Here we extend those studies by considering all of the particles of a given energy and including also the (2, 1) mode. It was shown in [15] that particles born at the same flux surface have a distribution of periods (bouncing and precession of trapped particles and toroidal and poloidal rotation of passing particles) and that the diffusion coefficient does not have sharp maxima at the frequencies corresponding to these periodic motions. Two reasons were proposed to explain this behaviour:

(i) Particles have random pitch angles and therefore there is a distribution of periods (frequencies) rather than a sharp peak, see figures 5 and 6 of [15].
(ii) Due to the perturbation, the type of particle orbit (trapped or passing) can change during the simulation, see figures 8 and 9 of [15] and the results presented below.

In the situation considered here, where particles have random pitch and are initially distributed inside the entire plasma according to the slowing down distribution function, the distribution of periods is similar for passing particles and broader for trapped particles (both for the bouncing and precession periods) when compared with those shown in [15]. We therefore expect an even smoother frequency dependence.

A pseudo-diffusion coefficient was introduced in [15] to quantify the departure of the alpha particles from the original flux surface. Here it is important to see how the initially peaked alpha particle density spreads out due to the interaction with the modes present in a sawtooth. The width of the alpha particle distribution can be characterized by $\sigma^2(t)$, defined as

$$\sigma^2(t) = \frac{1}{N}\sum_i \left\{[r_i(t) - \bar{r}(t)]^2 + [z_i(t) - \bar{z}(t)]^2\right\}, \qquad (5)$$

where $\bar{r}(t)$ and $\bar{z}(t)$ are the instantaneous averaged values of r and z (averaged over all the particles) and N is the total number of particles. To quantify the spreading of the alpha particles we introduce the parameter χ, defined as

$$\chi(t) = \frac{\sigma^2(t)}{\sigma^2(t=0)}. \qquad (6)$$

As already indicated, our simulations usually start when the (2, 2) and (2, 1) modes begin to grow and the (1, 1) mode is at 70% of its maximum amplitude. We assume that after the crash the amplitude of the modes decreases rapidly, in 15 μs. The (1, 1) mode decreases to 40% of its maximum value and the (2, 2) and (2, 1) modes to 20%. Since the simulations begin when the (1, 1) mode already has 70% of its maximum amplitude, the particles initially undergo a rapid redistribution to accommodate to the new magnetic field structure. To check the sensitivity of the results to the time history of the (1, 1) mode amplitude we performed other simulations where the (1, 1) mode starts with zero amplitude, grows with different slopes to the same maximum amplitude (see black curves in figure 3) and decays after the crash as before. Figure 4 shows a plot of χ as a function of time for three different cases ($\xi_0^{11} = 0.3$, $\xi_0^{22} = 0$, $\xi_0^{21} = 0$). Curve 1 was obtained starting with the (1, 1) mode at 70% (standard case); in curve 2 the mode amplitude starts from zero and grows in a time t_c and in curve 3 it grows in $2t_c$. Curve 1 clearly shows the initial redistribution but just before the crash the values of χ obtained with the three growth scenarios differ by less than 2%. The differences between the three cases increase after the crash (we do not know why yet) but remain below 6%. The results presented in figure 4 show that the final value of χ depends on the final amplitude of the mode and not on its time history. Additional evidence regarding this behaviour is shown in figure 5, which presents a plot of χ as a function of the amplitude of the (1,1) mode. Curve 1 is for the standard case (starts at 70%) and curves 2 and 3 (which are indistinguible) correspond to the same cases considered in the previous figure. We see again that for relative amplitudes above 70% (where case 1 starts) the differences are very small. We note that when the (1, 1) mode starts from zero, χ (and therefore σ^2) increases almost linearly in time until the crash occurs.

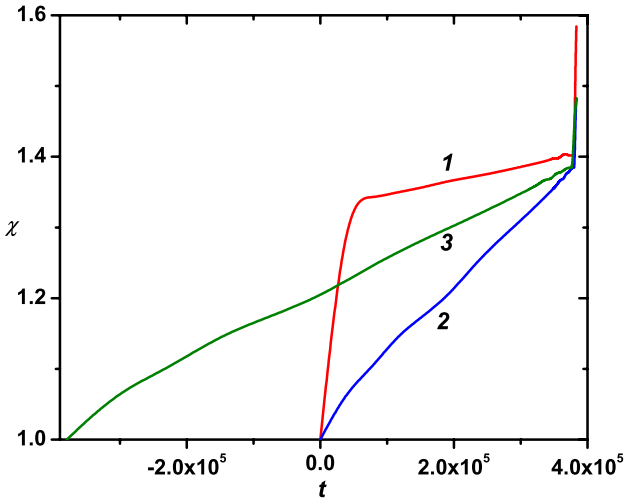

Figure 4. χ as a function of time for three different cases ($\xi_0^{11} = 0.3$, $\xi_0^{22} = 0$, $\xi_0^{21} = 0$). Curve 1 was obtained starting with the (1, 1) mode at 70% (standard case); in curve 2 the mode amplitude starts from zero and grows in a time t_c and in curve 3 it grows in $2t_c$. The numbers and colours of the curves correspond to the same scenarios indicated in figure 3.

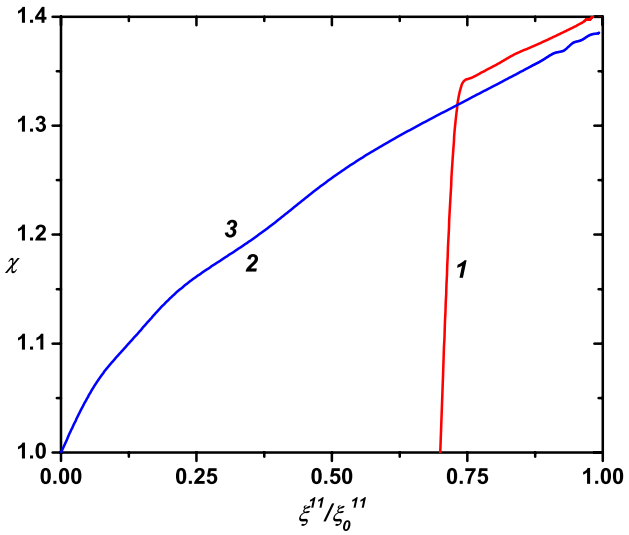

Figure 5. χ as a function of ξ^{11}/ξ_0^{11} for three different cases ($\xi_0^{11} = 0.3$, $\xi_0^{22} = 0$, $\xi_0^{21} = 0$). Curve 1 was obtained starting with the (1, 1) mode at 70% (standard case); in curve 2 the mode amplitude starts from zero and grows in a time t_c and in curve 3 it grows in $2t_c$.

4.1. Effect of modes (1,1) and (2,2)

We first analyse what occurs under the conditions reported in [12], where a (1, 1) mode with a maximum normalized amplitude of 0.12 and a (2, 2) mode with a maximum amplitude of approximately 1/3 that of the (1, 1) mode were found. The maximum perturbed magnetic field produced by these displacement amplitudes are $\delta B_{11} = 0.014$ and $\delta B_{22} = 0.004$, respectively. Figure 6 shows a plot of χ_f (final value of $\chi(t)$) as a function of the normalized frequency for $\xi_0^{11} = 0.12$, $\xi_0^{22} = 0$, and two energy values, $E = 3.5$ and 0.5 MeV. It is seen that the spreading (χ_f) of 3.5 MeV particles increases with the frequency up to $\omega \sim 2.5 \times 10^{-4}$, where

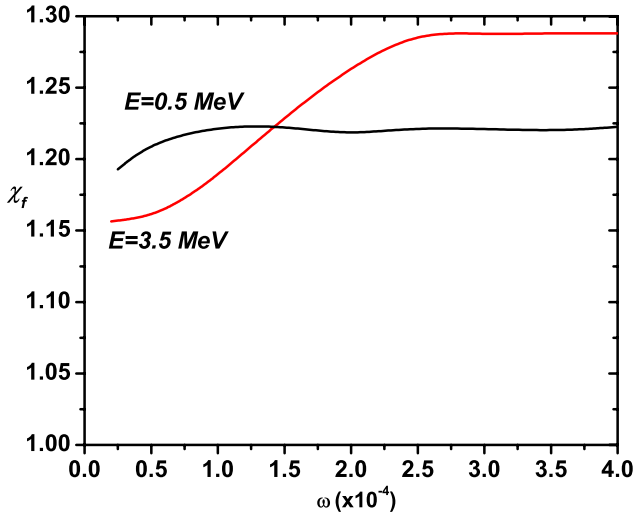

Figure 6. χ_f as a function of frequency for two energies. $\xi_0^{11} = 0.12$, $\xi_0^{22} = \xi_0^{21} = 0$.

it saturates. At lower energies ($E = 0.5$ MeV) χ_f remains approximately constant in the frequency range considered. Since the dependence is relatively weak, and there are many other parameters to change, we keep its value fixed at $\omega = 2 \times 10^{-4}$ in what follows.

Alpha particles can be divided into co-passing (rotate in the same sense as the current), counter-passing (rotate in the opposite sense) and trapped. This classification is not absolute because particles can change their status due to the interaction with the modes. In fact, we show below that the fraction of particles that change their status can be very significant, depending on the energy of the particles, amplitude of the perturbation, and modes present. We present below initial and final density profiles for the different groups of particles (co-passing, counter-passing, trapped). To construct these plots we considered the status of the particles at the time corresponding to the plot (initial or final). This means that the particles used to construct the density plots corresponding to a given group could be different. When analysing the effect of the perturbation on different groups of particles their initial (unperturbed) status is considered.

The effect of the perturbation is clearly different on different groups of particles. This can be seen in figure 7, which shows the initial and final density profiles for different groups of particles when $\xi_0^{11} = 0.12$, $\xi_0^{22} = 0$ and $E = 3.5$ MeV (full lines) and 0.5 MeV (dashed lines). The location of the $q = 1$ surface and the values of χ_f for the different groups of particles are also shown. In all cases the plots show the density as a function of radius (cylindrical coordinates) at $z = 0$. Counter-passing particles undergo a larger redistribution than co-passing particles while trapped particles are mostly shifted towards larger radius. Counter-passing particles of 0.5 MeV spread out more than 3.5 MeV particles, and the opposite occurs with trapped particles. The peak density of counter-passing particles decreases by approximately 40% for 0.5 MeV particles and 25% for 3.5 MeV particles. The peak density of trapped particles does not change very much but the position of the peak shifts outwards by approximately 10% of the minor radius (slightly more for 3.5 MeV particles). The spreading of co-passing particles is very small and similar for both energies.

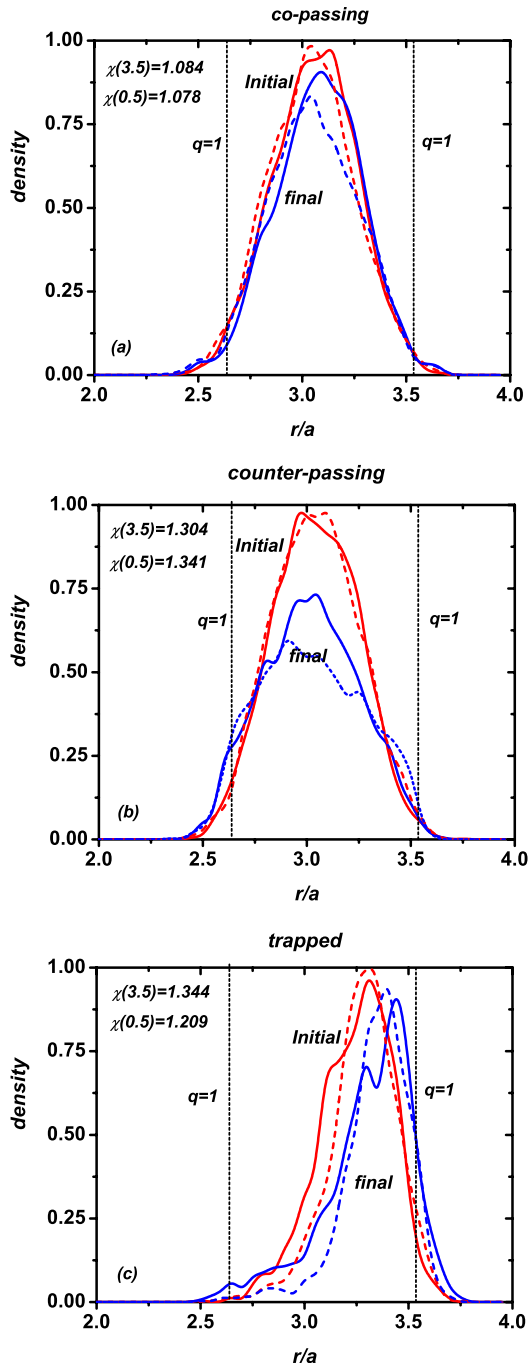

Figure 7. Density profiles for different groups of particles. Red lines for initial profiles and blue for final. Full lines for $E = 3.5$ MeV and dash lines for $E = 0.5$ MeV.

The total on axis density decreases by more than 25%. As expected, the density of alpha particles remains very small outside the $q = 1$ surface. The density profile of the trapped particles shows the presence of trapped particles on the high-field side of the magnetic axis (located at $r = 3.105$). This is due to the following reasons:

(i) Although the plot is supposed to show the density at $z = 0$, we are forced to collect particles located between $z = \pm 0.025$ to produce smooth enough histograms (with enough particles).

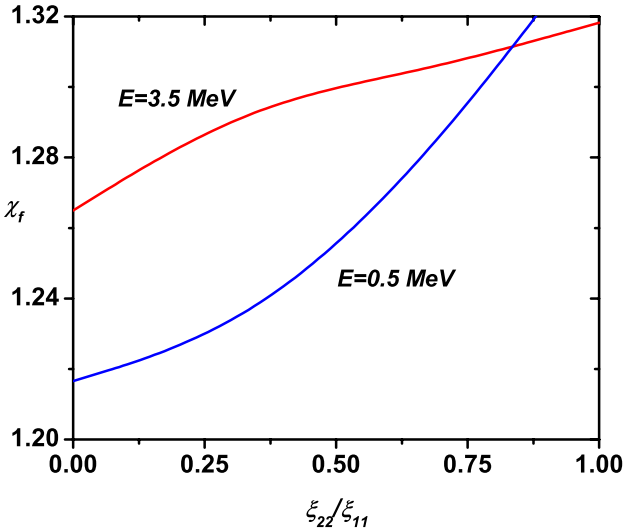

Figure 8. χ_f as a function of the ratio ξ_0^{22}/ξ_0^{11} for $\xi_0^{11} = 0.12$ and two different energies, $E = 3.5$ and 0.5 MeV.

(ii) Trapped particles in potato orbits can circle the magnetic axis due to drifts [29]. The fraction of these particles increases with energy, thus justifying that the fraction of trapped particles in the low-field side is larger for 3.5 MeV than for 0.5 MeV.

The difference between the response of counter-passing and co-passing particles can be qualitatively explained using the analysis presented in [30] (equations (1) and (2)). For our choice of phase $(m\theta - n\phi - \omega_{mn}t)$ the strongest resonance occurs at values of the safety factor given by

$$q_{\rm res} = \frac{m}{n + \frac{\omega_{mn}}{\omega_\phi}},$$

where ω_ϕ is the toroidal transit frequency. Since in our case $\omega_{mn} \ll \omega_\phi$ the resonance will be close to the $q = 1$ surface for the (1, 1) mode. Our equilibrium has the toroidal current anti-parallel to the toroidal magnetic field, which points in the positive toroidal direction. Co-passing particles therefore have a negative ω_ϕ while the opposite occurs for counter-passing particles. If ω_{11} is positive, $q_{\rm res} > 1$ for co-passing particles and $q_{\rm res} < 1$ for counter-passing particles. Since the amplitude of the (1, 1) mode decreases rapidly at the $q = 1$ surface it is substantially larger in the region where counter-passing particles resonate than in the region where co-passing particles resonate, thus explaining the stronger effect on the former. This explanation is further supported by the fact that if the sign of ω_{11} is changed, co-passing particles result more affected than counter-passing ones.

The addition of the (2, 2) mode does not change the value of χ_f significantly. This can be seen in figure 8, which shows a plot of χ_f as a function of the ratio ξ_0^{22}/ξ_0^{11} for $\xi_0^{11} = 0.12$ and two different energies, $E = 3.5$ and 0.5 MeV. The change in χ_f when the amplitude of the (2, 2) mode increases from zero to the value of the (1, 1) mode ($\xi_0^{22}/\xi_0^{11} = 1$) is approximately 10% for $E = 0.5$ MeV and less than 5% for $E = 3.5$ MeV.

Increasing the amplitude of the perturbations clearly results in a larger spreading. This is shown in figure 9, which presents a plot of χ_f as a function of the amplitude of the

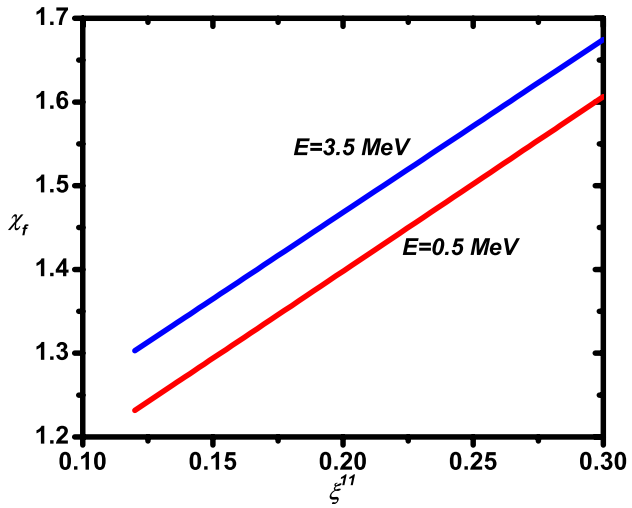

Figure 9. χ_f as a function of the amplitude of the (1, 1) and (2, 2) modes, $\xi_0^{22} = \xi_0^{11}/3$.

(1, 1) and (2, 2) modes, with $\xi_0^{22} = \xi_0^{11}/3$, and two different energies, $E = 3.5$ and 0.5 MeV. It can be seen that χ_f increases almost linearly with the amplitude of the perturbation and that higher energy particles are more strongly redistributed for this frequency value. The initial and final density profiles for each group of particles, for $\xi_0^{11} = 0.3$, $\xi_0^{22} = 0.1$, are shown in figure 10. The qualitative behaviour is similar to that shown in figure 7. Note that trapped 0.5 MeV particles have a larger χ_f than 3.5 MeV particles while the opposite occurs for counter-passing particles.

Although not shown here, particles with energies between 3.5 and 0.5 MeV display a very similar behaviour, with values of χ_f between those obtained for 3.5 and 0.5 MeV.

4.2. Effect of the (2,1) mode

The addition of the (2, 1) mode increases significantly the redistribution of alpha particles. When analysing the effect of this mode it should be noted that the perturbed magnetic field produced by a (2,1) mode with $\xi_0^{21} = 0.04$ has a maximum value of $\delta B_{21} = 0.012$, which is similar to the value obtained with a (1,1) mode having $\xi_0^{11} = 0.12$.

As indicated above, regions of stochasticity appear when the (2,1) mode is included. This is shown in figure 11, which presents Poincaré plots for three different conditions. Figure 11(*a*) has only the (1,1) mode ($\xi_0^{11} = 0.12$); figure 11(*b*) has the (1,1) and (2,2) modes ($\xi_0^{11} = 0.12$, $\xi_0^{22} = 0.04$) and figure 11(*c*) has the (1,1), (2,2) and (2,1) modes ($\xi_0^{11} = 0.12$, $\xi_0^{22} = 0.04$, $\xi_0^{21} = 0.04$). With the (1,1) and (2,2) modes the corresponding island structure appears but there are no signs of stochastic behaviour. When the (2,1) mode is included a large stochastic region appears.

Figure 12 presents a plot of χ_f as a function of the ratio ξ_0^{21}/ξ_0^{11} for $\xi_0^{11} = 0.12$, $\xi_0^{22} = 0.04$ (red lines) and $\xi_0^{11} = 0.3$, $\xi_0^{22} = 0.1$ (blue lines), and two values of energy: $E = 3.5$ MeV (full lines) and $E = 0.5$ MeV (dashed lines). It is clear that adding the (2, 1) mode increases the spreading significantly (almost linearly with the amplitude) but its quantitative effect depends on the energy of the particles and the amplitude of the perturbation. Lower energy particles are generally more

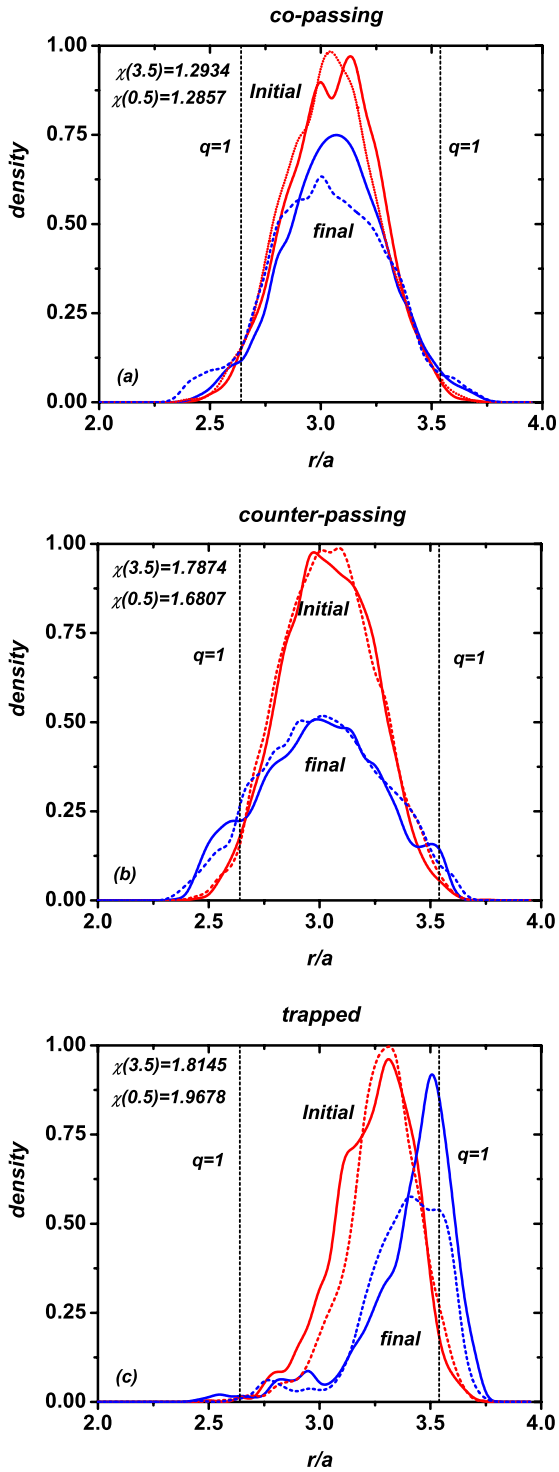

Figure 10. Density profiles for different groups of particles. Red lines for initial profiles and blue for final. Full lines for $E = 3.5$ MeV and dash lines for $E = 0.5$ MeV. With $\xi_0^{11} = 0.3$, $\xi_0^{22} = 0.1$.

affected by the (2, 1) mode but the difference between 3.5 and 0.5 MeV particles is larger at lower mode amplitude. Also note that when the amplitude of the (2, 1) mode is very small higher energy particles are more affected, in agreement with the results shown above (without the (2, 1) mode).

The effect of changing the energy is also shown in figure 13, which presents a plot of χ_f as a function of the

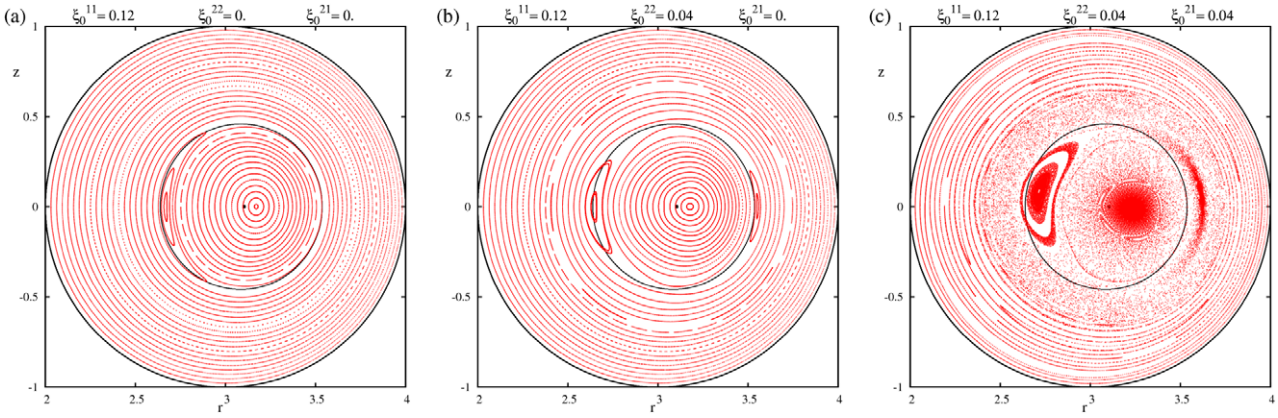

Figure 11. Poincaré plots for three different conditions. (*a*) has only the (1,1) mode ($\xi_0^{11} = 0.12$); (*b*) has the (1,1) and (2,2) modes ($\xi_0^{11} = 0.12$, $\xi_0^{22} = 0.04$) and (*c*) has the (1,1), (2,2) and (2,1) modes ($\xi_0^{11} = 0.12$, $\xi_0^{22} = 0.04$, $\xi_0^{21} = 0.04$). The inner black circumference indicates the position of the $q = 1$ surface.

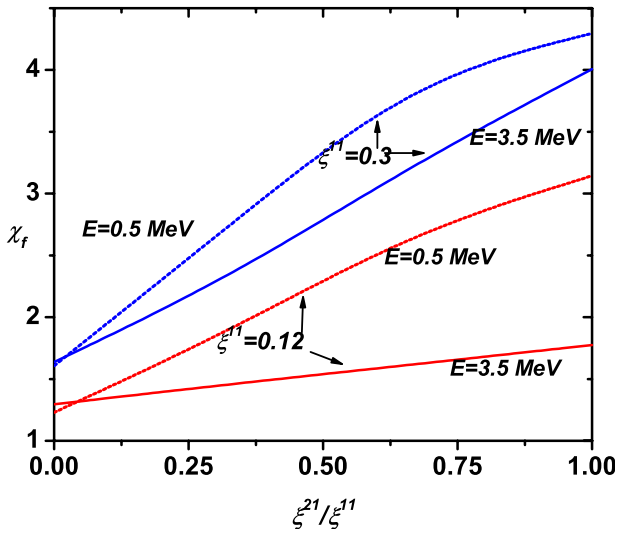

Figure 12. χ_f as a function of the amplitude of the (2,1) mode for different energies and amplitudes of modes (1,1) and (2,2). $\xi_0^{22} = \xi_0^{11}/3$.

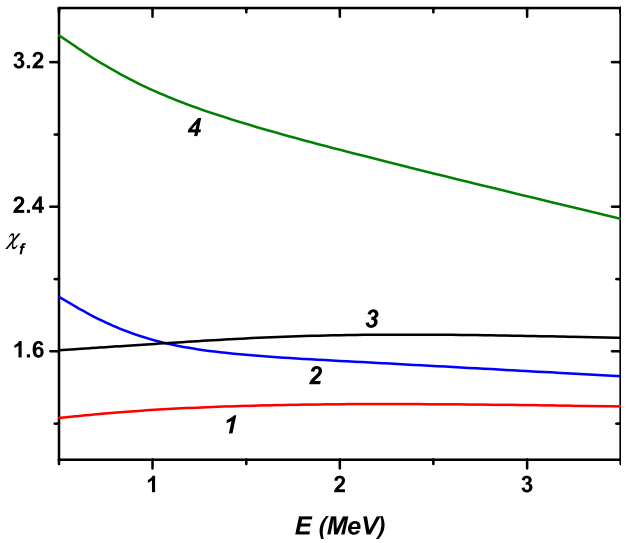

Figure 13. χ_f as a function of the energy for different mode amplitudes. The numbers on the curves correspond to the conditions shown in table 1.

Table 1. Amplitude of the modes for the curves of figure 13.

Curve	ξ_0^{11}	ξ_0^{22}	ξ_0^{21}
1	0.12	0.0	0.0
2	0.12	0.04	0.04
3	0.3	0.0	0.0
4	0.3	0.1	0.1

energy for different mode amplitudes. The mode amplitudes employed to obtain each curve are listed in table 1. It is clear that when the three modes are present lower energy particles are more affected and the relative change ($\chi_f(0.5)/\chi_f(3.5)$) increases with the amplitude of the modes (for the same relative amplitudes between the different modes).

In figure 14, we present plots of the initial and final densities of 3.5 MeV particles for $\xi_0^{11} = 0.12$ and 0.3, keeping the ratios ξ_0^{21}/ξ_0^{11} and ξ_0^{22}/ξ_0^{11} equal to 1/3 in all cases. It is interesting to note that although increasing the amplitude of the modes results in a larger spreading (the overall χ_f increases, as shown in figure 9), the result is very different for different groups of particles. Co-passing particles, which are hardly affected when $\xi_0^{11} = 0.12$, are strongly redistributed when $\xi_0^{11} = 0.3$. For counter-passing and trapped particles the effect of increasing the amplitude of the perturbation is less important.

When only the (1, 1) and (2, 2) modes are included, and the alpha particles are only weakly redistributed, the large electric field that appears at the crash produces a significant increase in χ. When the (2, 1) mode is included the particles undergo a significant redistribution before the crash (due to the stochasticity of the field lines) and the effect of the electric field at the crash is less important. This can be seen in figure 15, which shows the temporal evolution of χ, with (full line) and without (dash line) the perturbed electric field, for two different cases. In one case (red), only the (1, 1) mode is present while in the other (blue) the (2, 1) and (2, 2) modes were added. The sharp rise of χ at the crash is only seen when the perturbed electric field is included and the (2, 1) and (2, 2) are not present.

To conclude this analysis, we show, in table 2, the fraction of particles that change their status for different conditions.

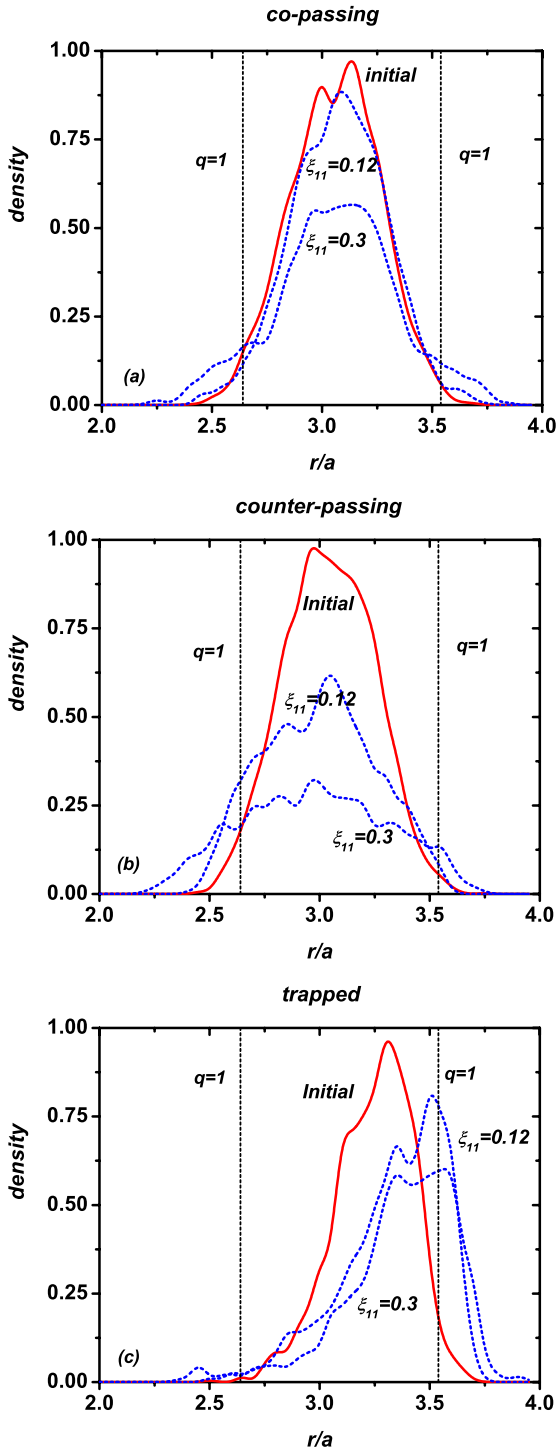

Figure 14. Initial and final densities of 3.5 MeV particles with $\xi_0^{11} = 0.12$ and 0.3. $\xi_0^{21}/\xi_0^{11} = \xi_0^{22}/\xi_0^{11} = 1/3$.

The different columns contain (from left to right): the case, energy, amplitude of the modes, initial and final percentages of particles of each type and the percentage of particles that changed status. The columns labelled (co-i and co-f) contain the initial and final percentages of co-passing particles, and similarly for counter-passing particles (ct-i, ct-f) and trapped particles (tr-i, tr-f). It is well known [31] that, due to an asymmetry in the passing–trapping boundary, the fractions of co-passing and counter-passing particles are different. We also note that only in case F, where all the modes are present with large amplitudes, the fraction of co-passing particles changes significantly.

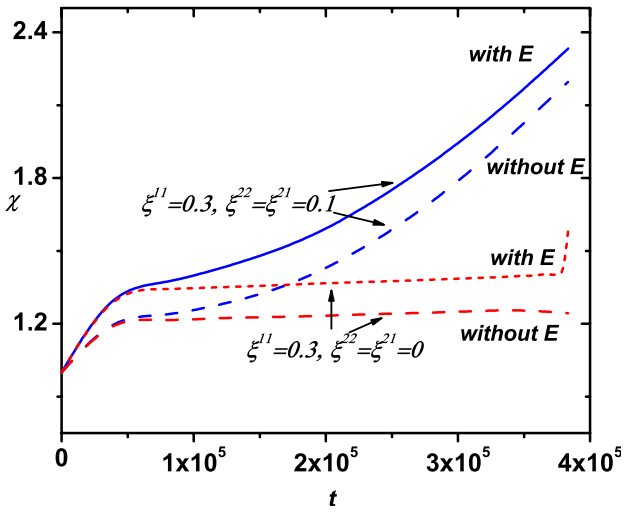

Figure 15. χ as a function of time with and without the electric field for different conditions. Blue curves have the three modes and red curves include only the (1,1) mode.

5. Summary and discussion

We investigated the effect of sawtooth oscillations on high energy alpha particles in plasmas with ITER-like parameters. The main results can be summarized as follows:

(i) For the conditions reported in [12] the peak density of counter-passing particles decreases between 25% and 40% (depending on the energy) and the peak of the trapped particles density shifts outwards by approximately 10% of the minor radius. The total on axis density decreases by more than 25%, indicating a significant reduction of the alpha particle heating in this region. The redistribution occurs inside the $q = 1$ surface.

(ii) The addition of a $(2, 1)$ mode, which can produce the stochastization of the magnetic field, significantly increases particle redistribution. It also allows particles to spread beyond the $q = 1$ surface. Its effect depends on the energy of the particles and the amplitude of the other modes.

(iii) For our conditions, counter-passing particles are more strongly redistributed than co-passing particles. However, the opposite occurs when the direction of mode propagation is changed. Trapped particles are also redistributed, they spread out and move towards larger radii.

(iv) The fraction of particles that change their status (from passing to trapped or vice versa), can be significant, depending on the energy and number and amplitude of the modes present.

(v) When only the $(1, 1)$ and $(2, 2)$ modes are present, and $\xi_0^{22} \leqslant 0.75\xi_0^{11}$, higher energy particles are more affected. When the $(2, 1)$ mode is included lower energy particles are more affected.

Table 2. Initial and final percentages of each type of particles and percentage of particles that changed their status for different conditions.

Case	E (MeV)	ξ_0^{11}	ξ_0^{22}	ξ_0^{21}	co-i	co-f	ct-i	ct-f	tr-i	tr-f	Change
A	3.5	0.12	0	0	41.3	41.3	34.5	33.2	24.2	25.5	6.1
B	0.5	0.12	0	0	39.2	38.8	36.4	35.5	24.4	25.7	9.3
C	3.5	0.12	0.04	0.04	41.3	41.2	34.5	31.3	24.2	27.6	14.7
D	0.5	0.12	0.04	0.04	39.2	38.6	36.4	29.3	24.4	32.1	25.0
E	3.5	0.3	0.1	0.1	41.3	41.1	34.5	28.0	24.2	31.4	36.9
F	0.5	0.3	0.1	0.1	39.2	37.9	36.4	28.1	24.4	33.9	48.0

(vi) Changing the time dependence employed during the growth of the (1, 1) mode does not change the results significantly if the maximum amplitude reached by the mode remains the same.

(vii) The large electric field that appears at the crash produces a significant change if the magnetic field does not become stochastic.

To remove some of the limitations of the model presented above we are developing a different approach, where the equilibrium and mode structure are calculated numerically. In this approach [32], an ITER-like equilibrium with $q_0 < 1$ is obtained by solving a 2D nonlinear Grad–Shafranov equation. This equilibrium is then used as the initial condition for a 3D, nonlinear resistive MHD simulation which determines the spatial structure of the modes. Preliminary results obtained with this method seem to be consistent with those presented above. A complete study of alpha particle redistribution using this approach will be presented in a future paper.

Acknowledgments

Financial support from the ECOS-MINCyT Research Grant No. A09E02 is gratefully acknowledged.

References

[1] Marcus F.B. *et al* 1991 *Plasma Phys. Control. Fusion* **33** 277
[2] Stratton B.C., Fonck R.J., McKee G.R., Budny R.V., Chang Z., Wising F. and Odblom A. 1996 *Nucl. Fusion* **36** 1586
[3] Nielsen S. *et al* 2010 *Plasma Phys. Control. Fusion* **52** 092001
[4] Muscatello C.M., Heidbrink W.W., Kolesnichenko Ya.I., Lutsenko V.V., Van Zeeland M.A. and Yakovenko Yu.V. 2012 *Plasma Phys. Control. Fusion* **54** 025006
[5] Nielsen S. *et al* 2011 *Nucl. Fusion* **51** 063014
[6] Muscatello C.M. *et al* 2012 *Nucl. Fusion* **52** 103022
[7] Kadomtsev B.B. 1976 *Sov. J. Plasma Phys.* **1** 389
[8] Kolesnichenko Y.I., Yakovenko Y.V., Anderson D., Lisak M. and Wising F. 1992 *Phys. Rev. Lett.* **68** 3881
[9] Porcelli F. *et al* 1996 *Plasma Phys. Control. Fusion* **38** 2163
[10] Letsch A., Zohm H., Ryter F., Suttrop W., Gude A., Porcelli F., Angioni C. and Furno I. 2002 *Nucl. Fusion* **42** 1055
[11] Igochine V., Boom J., Classen I., Dumbrajs O., Gunter S., Lackner K., Pereverzev G., Zohm H. and the ASDEX Upgrade Team 2010 *Phys. Plasmas* **17** 122506
[12] Igochine V., Dumbrajs O., Zohm H., Flaws A. and the ASDEX Team 2007 *Nucl. Fusion* **47** 23–32
[13] Udintsev V.S. *et al* 2005 *Plasma Phys. Control. Fusion* **47** 1111
[14] Zhao Y. and White R.B. 1997 *Phys. Plasmas* **4** 1103
[15] Farengo R., Ferrari H.E., Firpo M.-C., García-Martínez P.L. and Lifschitz A.F. 2012 *Plasma Phys. Control. Fusion* **54** 025007
[16] Kolesnichenko Y.I. and Yakovenko Y.V. 1992 *Nucl. Fusion* **32** 449
[17] Kolesnichenko Y.I. and Yakovenko Y.V. 1996 *Nucl. Fusion* **36** 159
[18] Kolesnichenko Y.I., Lutsenko V.V., White R.B. and Yakovenko Y.V. 2000 *Nucl. Fusion* **40** 1325
[19] Kolesnichenko Y.I., Lutsenko V.V., White R.B. and Yakovenko Y.V. 2001 *Phys. Lett.* A **287** 131
[20] Firpo M.C. and Constantinescu D. 2011 *Phys. Plasmas* **18** 032506
[21] Freidberg J.P. 1987 *Ideal Magneto Hydrodynamics* (New York: Plenum) Chapter 9
[22] Terry P.W. 2000 *Rev. Mod. Phys.* **72** 109
[23] Estrada-Mila C., Candy J. and Waltz R.E. 2006 *Phys. Plasmas* **13** 112303
[24] Bosch H.S. and Hale G.M. 1992 *Nucl. Fusion* **32** 611
[25] Doyle E.J. *et al* 2007 *Nucl. Fusion* **47** S18
[26] Berland J., Bogey C. and Bailly C. 2006 *Comput. Fluids* **35** 1459
[27] Fasoli K.A., Goodman T.P. and the TCV Team 2007 *Plasma Phys. Control. Fusion* **49** L1
[28] Wesson J. 2004 *Tokamaks* 3rd edn (Oxford: Clarendon) p 368
[29] White R.B. 2001 *The Theory of Toroidally Confined Plasmas* 2nd edn (London: Imperial College Press) Chapter 3
[30] White R.B., Gorelenkov N., Heidbrink W.W. and Van Zeeland M.A. 2010 *Phys. Plasmas* **17** 056107
[31] Chu T.K. 1996 *Phys. Plasmas* **3** 3397
[32] Farengo R., Ferrari H.E., Firpo M.-C. and García-Martínez P.L., Ettoumi W. and Lifschitz A.F. 2012 *24th IAEA Fusion Energy Conf. (San Diego, CA, 8–13 October)* paper TH-P6/4 www-naweb.iaea.org/napc/physics/FEC/FEC2012/html/fec12.htm